Revealing topological Dirac fermions at the surface of strained HgTe thin films via Quantum Hall transport spectroscopy

C. Thomas, O. Crauste, B. Haas, Pierre-Henri Jouneau, Christopher Bäuerle, L. P. Levy, Edmond Orignac, D. Carpentier, P. Ballet, Tristan Meunier

Revealing topological Dirac fermions at the surface of strained HgTe thin films via quantum Hall transport spectroscopy

C. Thomas,[1] O. Crauste,[2,3] B. Haas,[4] P.-H. Jouneau,[4] C. Bäuerle,[2,3] L. P. Lévy,[2,3] E. Orignac,[5] D. Carpentier,[5] P. Ballet,[1] and T. Meunier[2,3]

[1]*Université Grenoble Alpes, CEA, LETI, MINATEC campus, F38054 Grenoble, France*
[2]*CNRS, Institut NEEL, F-38042 Grenoble, France*
[3]*Université Grenoble Alpes, Institut NEEL, F-38042 Grenoble, France*
[4]*Université Grenoble Alpes, CEA, INAC, F38054 Grenoble, France*
[5]*Université Lyon, ENS de Lyon, Université Claude Bernard, CNRS, Laboratoire de Physique, F-69342 Lyon, France*

(Received 27 April 2017; revised manuscript received 21 November 2017; published 21 December 2017)

We demonstrate evidences of electronic transport via topological Dirac surface states in a thin film of strained HgTe. At high perpendicular magnetic fields, we show that the electron transport reaches the quantum Hall regime with vanishing resistance. Furthermore, quantum Hall transport spectroscopy reveals energy splittings of relativistic Landau levels specific to coupled Dirac surface states. This study provides insights in the quantum Hall effect of topological insulator (TI) slabs, in the crossover regime between two- and three-dimensional TIs, and in the relevance of thin TI films to explore circuit functionalities in spintronics and quantum nanoelectronics.

DOI: 10.1103/PhysRevB.96.245420

I. INTRODUCTION

Similar to the case of graphene, the charge carriers at the surface of topological insulators are expected to be massless Dirac fermions but with a real spin locked to the momentum [1–3]. This has strong implications when the electrons experience a large perpendicular magnetic field B and enter the quantum Hall regime. Indeed, each surface is then characterized by nondegenerate Landau levels (LLs) and the associated Hall conductance is expressed as $\sigma_{xy} = (N + \frac{1}{2})\frac{e^2}{h}$, where N is the LL index. In topological insulator slabs, however, two surface states of extension w have to be considered and are separated by a thickness t. When the wave functions of the two surfaces do not overlap ($t \gg w$), they are only connected at the boundaries of the sample [4] and the transport properties are obtained by summing the distinct contributions of each surface. The Hall conductance $\sigma_{xy} = (N_{\text{top}} + N_{\text{bottom}} + 1)\frac{e^2}{h} = \nu\frac{e^2}{h}$ is then expected where N_{top} and N_{bottom} are the LL index for the top and bottom surfaces, respectively. In this regime, integer filling factors ν have been observed in relatively thick strained HgTe [5–7] and Bi-based [8,9] topological insulators. By decreasing t down to w, the two surface states start to overlap giving rise to a non-negligible hybridization energy Δ [10–12] and the transport then occurs through states delocalized between the two coupled surfaces. In this regime, degenerate Dirac LLs are expected to emerge at high B with energies scaling as $\sqrt{NB}$. Moreover, additional dispersive couplings between the two surfaces are expected to lift the LL degeneracy with an energy splitting linear in B [12,13]. While of orbital nature, this splitting reveals the microscopic coupling of spin and orbital degrees of freedom in the Dirac Landau levels. Therefore analyzing the energy gaps of both odd and even filling factors and their B dependencies provides a powerful tool to experimentally reveal the Dirac surface states of a thin topological insulator slab. Decreasing further t would result in the opening of a large gap in the surface states and the emergence of the quantum spin Hall phase [11–14].

In this paper, the magnetotransport properties of strained HgTe thin films at high magnetic fields are investigated. We study films with a thickness of about 15 nm, comparable with surface-state wave function penetration length [15], thus characterized by two tunnel-coupled surfaces where electronic transport is solely mediated by surface charge carriers. The quality of the material allows reaching the quantum Hall regime with vanishing resistance for magnetic field larger than 1.5 T. At higher magnetic fields, nondegenerate Landau levels are observed. By analyzing the temperature dependence of the magnetoconductance, a clear difference of the energy gaps corresponding to odd and even filling factors is noticed and is consistent with a Landau-level energy spectrum characteristic of two coupled Dirac surfaces.

II. EXPERIMENT

A. Sample and low magnetic field characterization

We investigate top-gated Hall bars [see Fig. 1(a)] fabricated from a 15-nm-thick HgTe layer surrounded by two 30-nm-thick $Hg_{0.3}Cd_{0.7}Te$ barriers and grown on a (100) CdTe substrate. Particular attention to lower the defects present in the HgTe layer and to obtain sharp $HgTe/Hg_{0.3}Cd_{0.7}Te$ interfaces was paid during the structure growth [16] [see Fig. 1(b)]. Two different structures with similar thickness were grown and gave very similar results. The Hall bar is 40 μm long and 10 μm wide. A top gate covering the Hall bar enables us to change the carriers from holes to electrons as illustrated by the density sign inversion in Fig. 1(c). It is worth noting that the ohmic contacts to the surface states become highly resistive at high magnetic fields, and as a consequence only magnetotransport properties up to 3 T are reported.

In HgTe layers, the light-hole band $\Gamma_{8,\text{LH}}$ band is lying 0.3 eV above the Γ_6. Such an inverted band structure at the Γ point results in topological surface states, robust to the presence of the heavy-hole band $\Gamma_{8,\text{HH}}$ [17]. At zero magnetic field and close to the charge neutrality point, the longitudinal resistance R_{xx} presents a peak at gate voltage V_{DP}

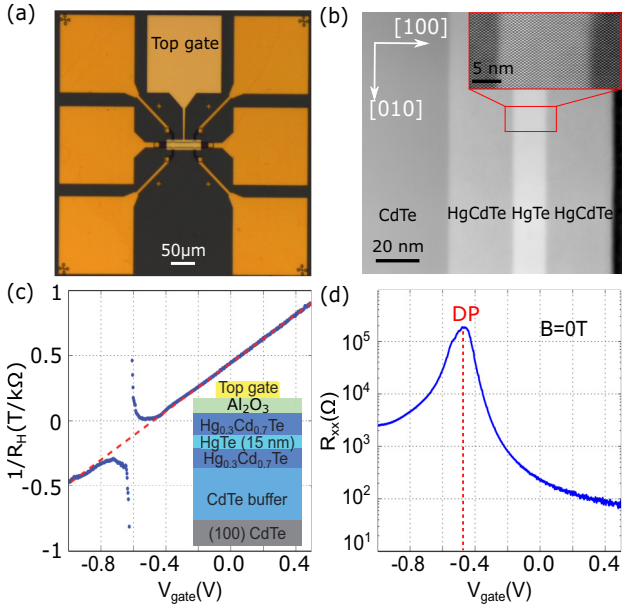

FIG. 1. (a) Optical image of the Hall bar sample realized after nanofabrication of the structure. (b) Scanning transmission electron microscopy (STEM) image in a high angle annular dark field (HAADF) mode of a 15-nm-thick HgTe layer embedded between two $Hg_{0.3}Cd_{0.7}Te$ barriers. Inset: High-resolution STEM HAADF image zooming on the HgTe layer. Low defect density and quality of the interfaces are evidenced. (c) Evolution of the slope $R_H = \frac{dR_{xy}}{dB}$ at low perpendicular magnetic fields with the voltage V_{gate} applied on the gate. In a one-carrier model, the density n is equal to $\frac{1}{eR_H}$ where e is the charge of an electron. V_{gate} adjusts n in the range of order of 10^{11} cm^{-2}. The red dashed line corresponds to a fit, which allows us to extract the depleting factor of the gate α equal to $\sim 5 \times 10^{11}$ cm^{-2} V^{-1}. Inset: Schematics of the strained HgTe topological insulator structure used in the experiment. (d) Longitudinal resistance R_{xx} as a function of V_{gate} at zero magnetic field showing the Dirac point at $V_{\text{gate}} = V_{\text{DP}} \sim -0.5$ V.

[see Fig. 1(d)], whose amplitude depends on the size of the sample and can be as low as 1 kΩ for Hall bars of 1 micrometer [18]. We conclude that the structure has a metallic behavior as expected for electron transport through surface states.

B. Demonstration of the quantum Hall effect

To probe the nature of the surface-state carriers, we analyze the Hall bar magnetoconductance at high perpendicular magnetic fields and at a temperature of 100 mK. Shubnikov–de Haas (SdH) oscillations on R_{xx} and quantized plateaus on the Hall resistance R_{xy} are observed [see Figs. 2(a) and 2(b)] and point at the emergence of LLs in the structure. Both B and the top gate voltage V_{gate} allow controlling the filling of individual LLs. Indeed, the carrier density n is directly related to B and V_{gate} through $n = \alpha V_{\text{gate}} = \nu \frac{eB}{h}$ where α is the depleting factor of the gate [see Fig. 1(c)]. Derived from the extracted electron density at low B, the expected positions of the R_{xx} minima are represented by the black dashed lines in Fig. 2(a). They are reproducing properly the minima of the fan diagram considering only odd filling factors on the hole side ($V_{\text{gate}} \leqslant V_{\text{DP}}$) and both even and odd integers on the electron side

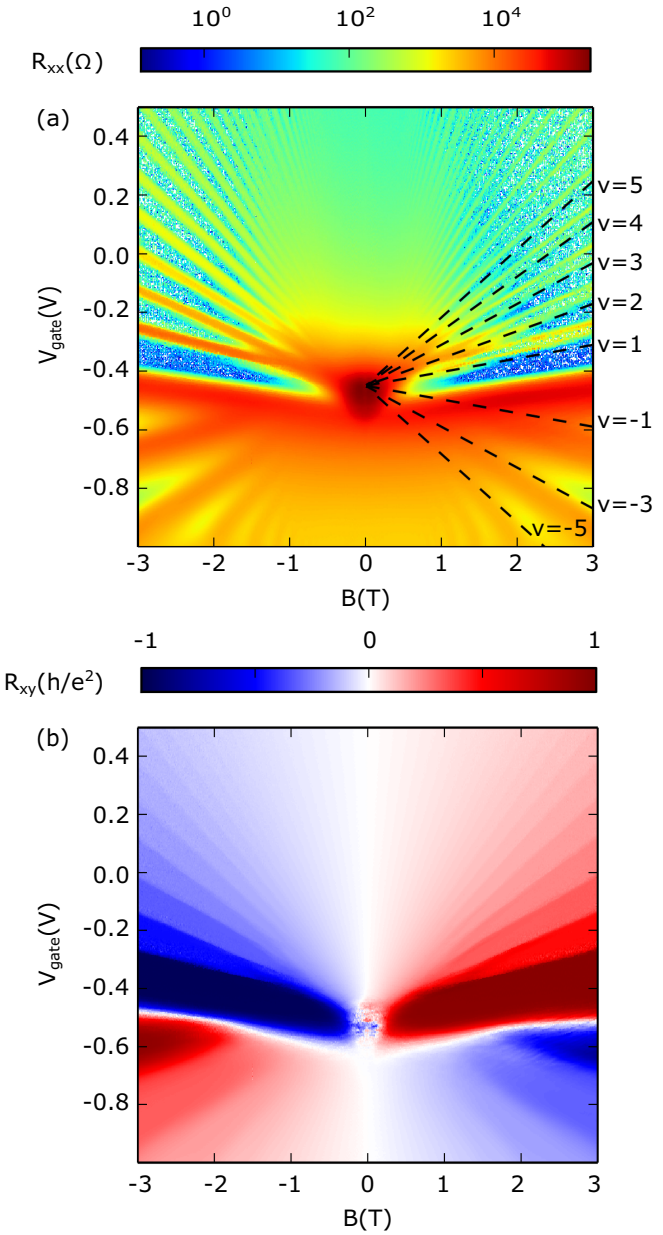

FIG. 2. (a) Longitudinal resistance R_{xx} as a function of V_{gate} and the perpendicular magnetic field B at 100 mK. The dashed lines represent the expected position of the R_{xx} minima extracted from the density evolution with V_{gate} [see Fig. 1(c)]. (b) Hall resistance R_{xy} (in units of $\frac{h^2}{e}$) as a function of V_{gate} and B.

($V_{\text{gate}} \geqslant V_{\text{DP}}$), in agreement with the corresponding quantized plateaus on the R_{xy} mapping on Fig. 2(b).

At $B = \pm 3$ T, the quantum Hall regime is achieved on the electron side with vanishing resistance and Hall conductance plateaus corresponding to integer filling factors (see Fig. 3). Such observations are strong signatures that there is no extra bulk contribution to the transport in the electron regime, contrary to what is observed in thicker samples [5–7]. On the hole side, σ_{xy} plateaus corresponding to odd filling factors are observed with σ_{xx} no longer completely vanishing. Moreover, it is worth noticing that σ_{xx} is characterized by broader peaks than on the electron side.

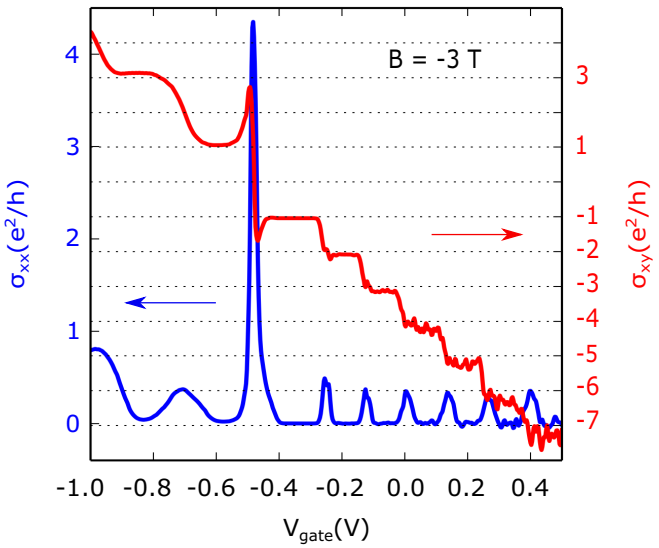

FIG. 3. The Hall $\sigma_{xy} = \frac{\rho_{xy}}{\rho_{xy}^2+\rho_{xx}^2}$ and the longitudinal $\sigma_{xx} = \frac{\rho_{xx}}{\rho_{xy}^2+\rho_{xx}^2}$ conductances as a function of V_{gate} for $B = -3$ T with $\rho_{xy} = R_{xy}$ and $\rho_{xx} = R_{xx}\frac{W}{L}$, L and W respectively the length and the width of the Hall bar.

The observed differences between holes and electrons are explained by the coupling of the surface states with the heavy-hole $\Gamma_{8,\text{HH}}$ bulk band. From the band structure of strained HgTe [17], the $\Gamma_{8,\text{HH}}$ band is expected to efficiently couple to the hole part of the surface states. This coupling opens up scattering channels resulting in the increased broadening of σ_{xx} peaks. The LL broadening is determined using the amplitude dependence of the SdH oscillations as a function of the magnetic field using the relation

$$\frac{\Delta R_{xx}}{4R_0} = \gamma_{th} \exp\left(-\frac{\pi}{w_c \tau_q}\right), \tag{1}$$

where ΔR_{xx} is the amplitude of the SdH oscillations, R_0 is the resistance background of the oscillations, γ_{th} describes the temperature effect on the LL broadening, τ_q is the quantum scattering lifetime, and $w_c = \frac{eB}{m^*}$ is the cyclotron frequency. The cyclotron effective mass m^* has been determined using the relation $m^* = \frac{\hbar\sqrt{\pi n}}{v_f}$ [19], where v_f is the surface-state band velocity equal to 5×10^5 m s^{-1} in our structures [17].

Figure 4(a) displays the evolution of the broadening $\Gamma_e = \frac{\hbar}{2\tau_q}$ in the electron side as a function of the gate voltage. Note that Γ_e is decreasing with V_{gate}. This behavior is consistent with R_{xx} mapping of Fig. 2(a) where we can see that the closer the LLs are from the Dirac point, the more important the magnetic field value is at which the splitting appears. This is especially visible with the $\nu = 2$ plateau appearing for $|B| \geqslant 1.5$ T while $\nu = 4$ shows up at larger gate voltage value for $|B| \geqslant 1.0$ T. Due to a non-negligible bulk contribution in the hole side, a similar analysis in this regime has not been possible. However, to have an estimation of the broadening, we have fitted $N = 1$ and $N = -1$ LL peaks with a Gaussian distribution to extract the full width at half maximum [see inset of Fig. 4(b)]. Figure 4(b) demonstrates the difference through the ΔV_{gate} values between hole and electron peaks.

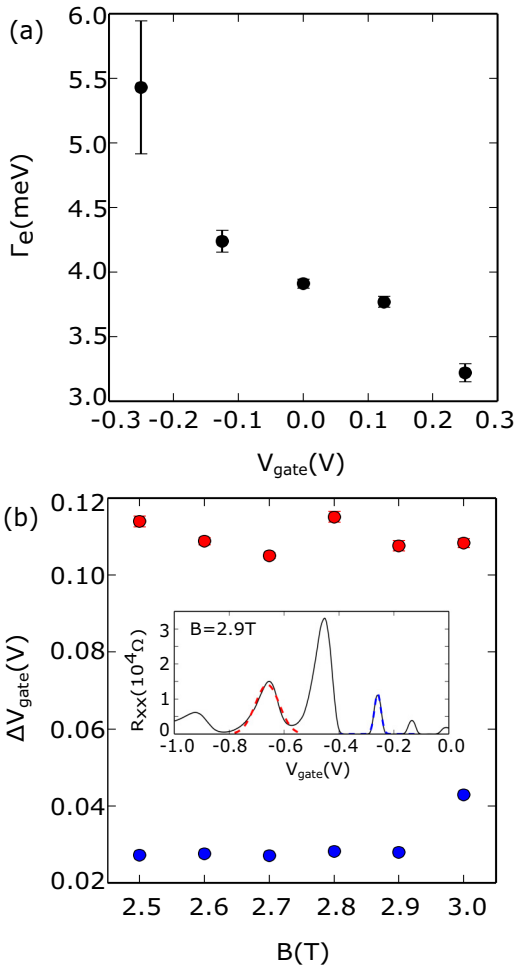

FIG. 4. Estimation of the Landau-level broadening on the electron and the hole sides. (a) Determination of the LL energy broadening Γ_e as a function of V_{gate} in the electron side. (b) Estimation of the energy broadening Γ_h on the hole side using comparison between the full width at half maximum ΔV_{gate} of the R_{xx} peaks for the $N = 1$ (blue) and $N = -1$ (red) peaks (shown in the inset) as a function of B.

With a ratio of about 3.7, the hole broadening Γ_h has been estimated to be larger than 11 meV. More precise determination of Γ_h is complicated as it would also depend on the gate voltage.

As a consequence of $\Gamma_h \gg \Gamma_e$, a larger magnetic field is needed on the hole side to resolve the observed spin splitting on the electron side. Whereas the $\nu = 2$ plateau is obtained for $|B|$ larger than $\sim$1.5 T with a clear separation of the R_{xx} maxima into two distinct branches [see Fig. 2(a)], additional measurements on a second sample with ohmic contacts working up to 5.5 T allow detecting the $\nu = -2$ plateau on the hole side only when B equals 5 T [18]. We can thus conclude that only one set of fan diagrams, associated to the same surface state on both electron and hole sides, is observed in the quantum Hall regime. Moreover, the degeneracy of the Landau levels is lifted for a 15-nm-thick HgTe topological film at high perpendicular magnetic fields.

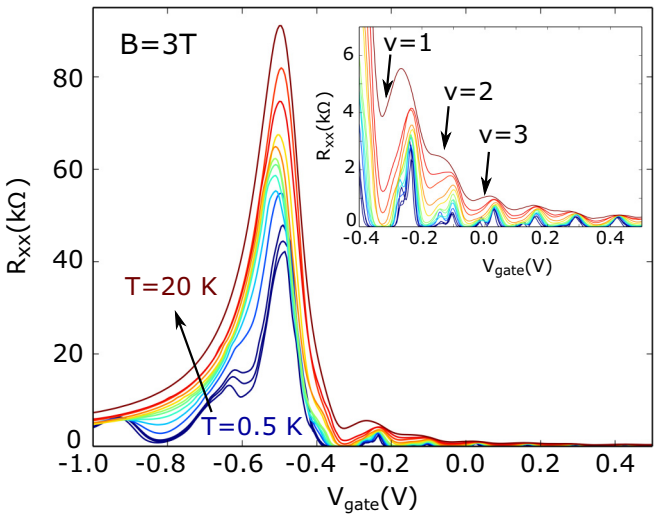

FIG. 5. R_{xx} as a function of V_{gate} for temperatures T ranging from 0.5 to 20 K and at $B = 3$ T. The inset is a zoom on the electron side. The thermally activated behavior of R_{xx} minima is evidenced.

C. Quantum Hall transport spectroscopy

To gain knowledge on the nature of the Landau levels, we analyzed the temperature dependence of the magnetoconductance in the quantum Hall regime [20–22]. In such a procedure, the energy difference between LLs is estimated via thermal activation. More precisely, the temperature dependence of the longitudinal resistance R_{xx} minima (see Fig. 5) is fitted using the Arrhenius law [see Fig. 6(a) for $\nu = 1$]: $R_{xx}^{min} \propto \exp\left(\frac{-\Delta E}{2k_B T}\right)$ where ΔE is the activation energy gap, k_B the Boltzmann constant, and T the temperature. Figure 5 displays the quantum Hall effect measurements performed for temperatures rising from the mK range up to 20 K. As expected, the resistance minima are increasing with temperature. One can notice that they are still visible at 20 K in the electron side while they disappear around $T = 4$ K in the hole side. Such difference is interpreted as the impact of the $\Gamma_{8,\text{HH}}$ bulk band on the hole side. This analysis has thus only been performed on the electron side. We first focus on odd filling factors where two successive LLs have different orbitals [see Figs. 6(b) and 6(c)]. We clearly observe nonregular energy separations between the successive LLs. Indeed, they decrease with N and increase nonlinearly with B (mostly noticed for the $\nu = 1$ gap). Both observations are in qualitative agreement with a Dirac-like LL energy spectrum scaling as $\sqrt{NB}$.

The resulting energy gaps for even filling factors do not show the same behavior [see Fig. 6(d)]. Indeed, the activation energy gaps for all these LLs are similar and linear with B. The slope 2β has been estimated to be about 2.07 ± 0.65 meV/T from the red solid line fit of Fig. 6(d), which is similar to the Landau-level splitting observed in HgTe nontopological quantum wells [23,24].

To quantitatively model the energy gaps for odd and even filling factors, we consider an effective low-energy model of a thin 3D topological insulator. From the two-dimensional (2D) quantum well point of view, the increased thickness of our 15-nm sample leads to additional bands [25]. Out of these bands two of them correspond to the top and bottom surface states while the others are confined bulk bands of a 3D topological insulator [27]. The low-energy transport properties of the sample will thus be dominated by these two overlapping surface bands with opposite chirality $\hbar v_f \tau_z(\sigma_x k_y - \sigma_y k_x)$ coupled by a k-dependent hopping amplitude of $(\frac{\Delta}{2} - \frac{k^2}{2M})\tau_x$. This coupling is purely of orbital nature, it does not depend on spins, and originates from the overlap of the two surface states that opens a constant gap Δ and introduces a quadratic $\frac{k^2}{2M}$ hopping amplitude [12]. In these conditions, we obtain the

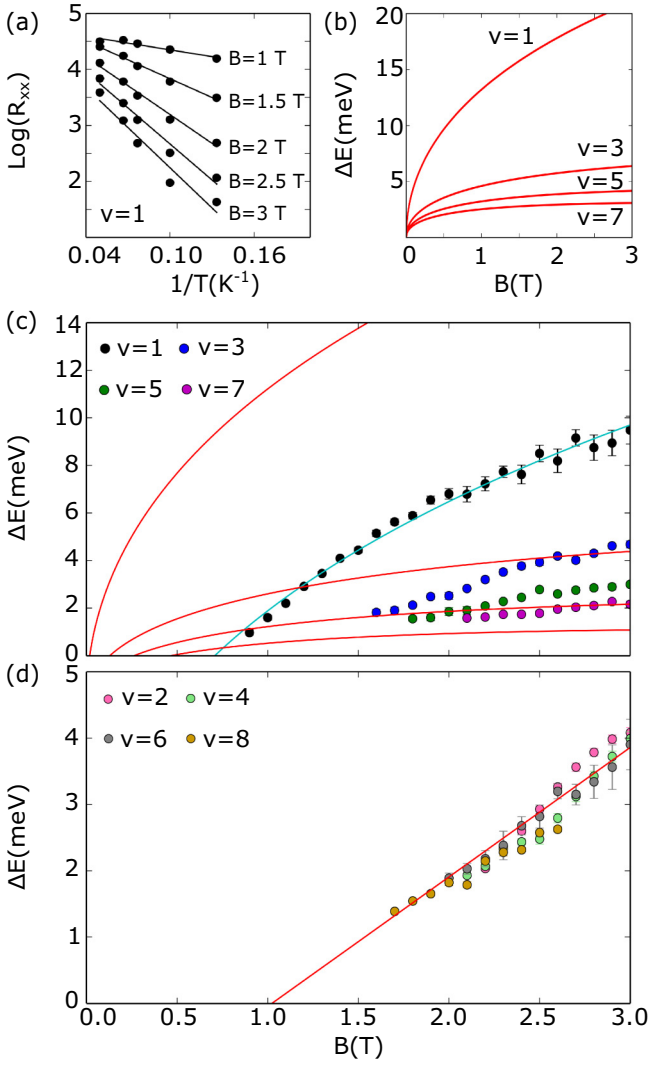

FIG. 6. Minimum of R_{xx} as a function of temperature T for the ν=1 filling factor. (a) This analysis allows to extract the activation energy gap ΔE for all positive filling factors at different B. ΔE evolution with B for odd filling factors $\nu = 1,3,5$ and 7: (b) from the model of eq. 2 and 3: $\Delta E_{\nu=2N+1} = E_{N+1,-} - E_{N,+}$, (c) from the experimental data. (d) ΔE as a function of B for even filling factors. In (c) and (d), the red solid lines represent the result of the model $\Delta E_{\nu=2N+1} = E_{N+1,-} - E_{N,+} - \Gamma$ and $\Delta E_{\nu=2N} = E_{N,+} - E_{N,-} - \Gamma$, respectively, with a constant offset $\Gamma = 3$ meV (see text). In (c), the blue solid line shows the result of the model with a larger offset of Γ= 11 meV, in better agreement with the data for ν=1.

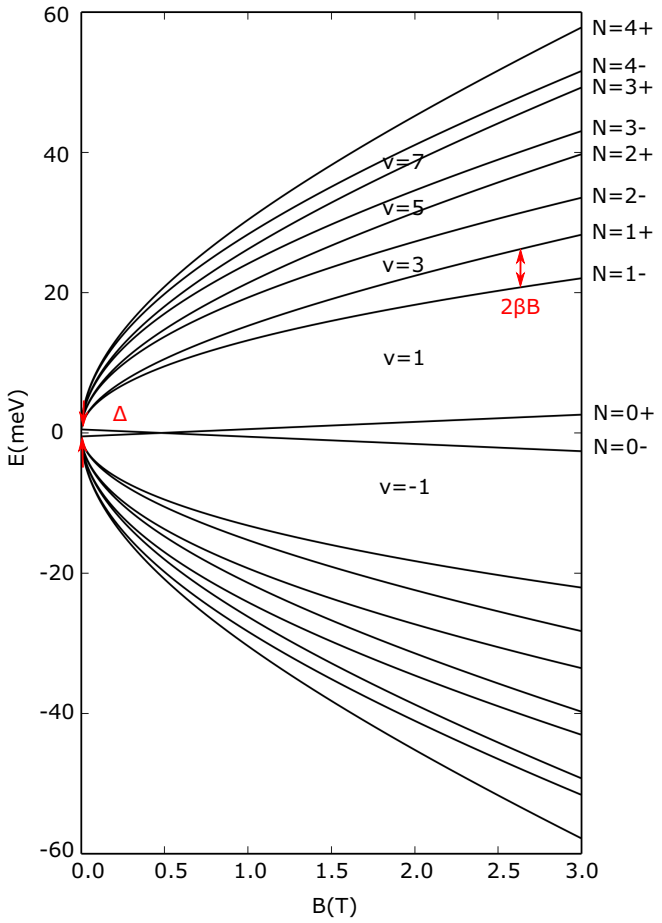

FIG. 7. Energy spectrum as a function of magnetic field for LL index N ranging from 0 to 4 on both electron and hole sides. LL splitting as well as hybridization gap Δ are evidenced. Δ has been set to 2 meV, 2β to 2.07 meV/T, and v_f to $\approx 4 \times 10^5$ m s^{-1}.

following LL energy spectrum with $\beta = \frac{e}{2M}$ represented in Fig. 7 and explained in further detail in [18],

$$E_{N,\pm} = \pm\sqrt{2Ne\hbar v_f^2 B + \left(\frac{\Delta}{2} - N\beta B\right)^2} \pm \beta B, N \geqslant 1, \tag{2}$$

$$E_{0,\pm} = \pm\left|\beta B - \frac{\Delta}{2}\right|. \tag{3}$$

While of orbital nature, the term βB acts as an effective Zeeman energy and β is fixed by the analysis of the even filling factor energy gaps performed in the previous paragraph. This spectrum evidences a splitting of each orbital LL due to the presence of the quadratic term. It is worth noting that for a vanishing overlap between the two surfaces both the gap and the quadratic term go to zero and one should observe only odd filling factors [13]. The results of this model for the estimated v_f are presented in Figs. 6(b), 6(c), and 6(d) through the solid red lines. To obtain a good agreement between the data and the model for all energy gaps, we need to take into account the width of the Landau level Γ as an offset in energy.

As the filling of individual Landau level is carried by both magnetic field and gate voltage, it is difficult to make a direct relationship between one broadening value and one filling factor. Therefore to fit the activation energy gaps of Figs. 6(c) and 6(d) we choose to use a constant value of 3 meV to represent the broadening. We recognize that using this approximation, the quality of the fits is not optimal especially for $\nu = 3$, 5, and 7 but it definitely illustrates that the probed energy gaps are characterized by a nonconstant energy difference contrary to classical 2D electron gas.

Nevertheless, for $\nu = 1$, the model requires a three times larger $\Gamma = 11$ meV [solid blue line in Fig. 6(c)] that can be explained by the proximity in energy of the $\Gamma_{8,\mathrm{HH}}$ band [17]. Note that the model and the data are in good agreement for $\nu = 1$. We explain this better fit quality by the fact that the $\nu = 1$ plateau extends over a small range of gate voltages in comparison with the higher filling factors as can be seen in Fig. 2, and thus the broadening correction needed for this filling factor does not significantly vary with B.

These analyses point at the Dirac nature of the surface-state carriers of strained HgTe thin films.

III. CONCLUSION

In conclusion, we have shown that the quantum Hall regime with vanishing longitudinal resistance is achieved in 15-nm-thick strained HgTe layers. Dirac carriers are revealed via quantum Hall spectroscopy and solely propagate through states delocalized between the top and bottom topological surfaces of the HgTe slab. The overlap between the surface states results in the mixing of the two Dirac species and in the splitting of the Landau levels. Dirac-surface-restricted transport demonstrated on these strained HgTe thin films opens the route towards the realization of circuits with a particularly a large potential for spintronic applications as experimentally investigated in [26].

ACKNOWLEDGMENTS

We acknowledge N. Mollard for TEM sample preparation and the technical support from the technological centers of the Institut Néel, CEA-LETI, and PTA. T.M. acknowledges financial support from Fondation Nanoscience (Project No. FCSN 2012-01CE), Agence nationale de la recherche (Project No. ANR-12-BS04-0007-02), and European Research Council (Project No. 307149).

APPENDIX A: ADDITIONAL MEASUREMENTS ON A SECOND SAMPLE

To complete our analysis, we present here additional measurements made on a second sample (called sample 2 hereafter) for which ohmic contacts were reliable up to 5.5 T. The heterostructure design, the growth conditions, and nanofabrication steps are exactly the same between sample 2 and the one discussed in the main text (called sample 1 hereafter).

1. Metallic surface states

The gate dependence of R_{xx} was measured at zero magnetic field for several Hall bars with lengths L ranging from 1 to 40 μm keeping the aspect ratio constant. All the Hall bars considered in this section were fabricated from sample 2.

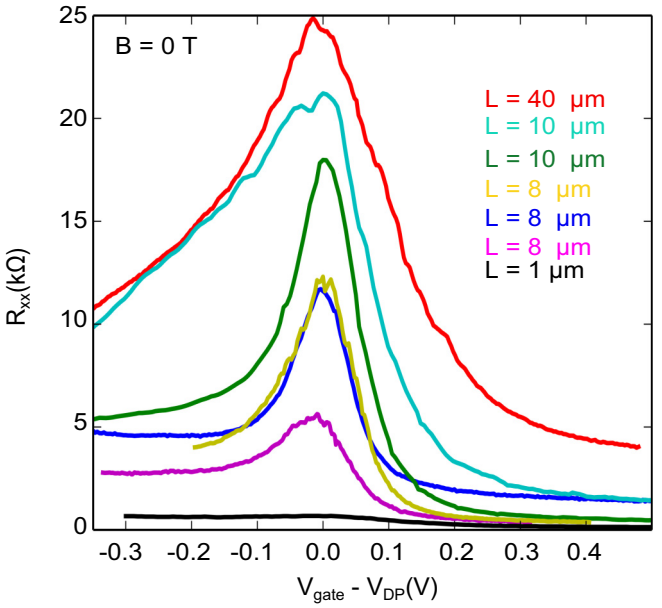

FIG. 8. Longitudinal resistance R_{xx} as a function of $V_{\text{gate}} - V_{\text{DP}}$ at zero magnetic field for sample 2. V_{DP} is defined for each curve as the voltage V_{gate} corresponding to the maximum R_{xx} and slightly varies from one Hall bar to another. The Hall bar length varies from 1 to 40 μm.

Similar observations were performed on sample 1. Figure 8 displays R_{xx} as a function of the gate voltage for $B = 0$ T and for T lower than 100 mK. For all the bars, R_{xx} evolves the same way as a function of the gate voltage V_{gate} and exhibits a maxima at the Dirac point (DP) for $V_{\text{gate}} = V_{\text{DP}}$. Resistance maxima are to first approximation increasing with L from 1 to 25 kΩ. This witnesses a nonballistic transport suggesting a metallic behavior of the surface states for which the resistance value is governed by scattering disorder potential. These observations are inconsistent with quantum spin Hall effect expected for thin HgTe topological quantum wells [14]. It is worth noting some divergences in the resistance of Hall bars of the same dimensions.

2. Experimental evidence of the Landau-level splitting in the hole side

In the main text, Hall bar magnetoconductance measurements were presented for magnetic fields up to 3 T where quantization between electron and hole side differs. All integer filling factors were observed in the electron side whereas only odd ones were observed for holes. Additional measurements have been performed for magnetic field values B up to 5.5 T on sample 2.

Figure 9 displays the longitudinal resistance R_{xx} as well as the Hall resistance R_{xy} as a function of B and V_{gate} for a Hall bar characterized by a length $L = 8$ μm and a width $W = 2$ μm at $T = 100$ mK. These two mappings unambiguously evidence the appearance of the $\nu = -2$ plateau for $B \geqslant 5$ T. This is emphasized in Fig. 10 where two traces of σ_{xy} for both $B = 3$ T and $B = 5.3$ T are displayed. A very clear and well defined $\nu = -2$ plateau exists for $B = 5.3$ T whereas for $B = 3$ T the quantization in the hole side jumps from -1 to -3.

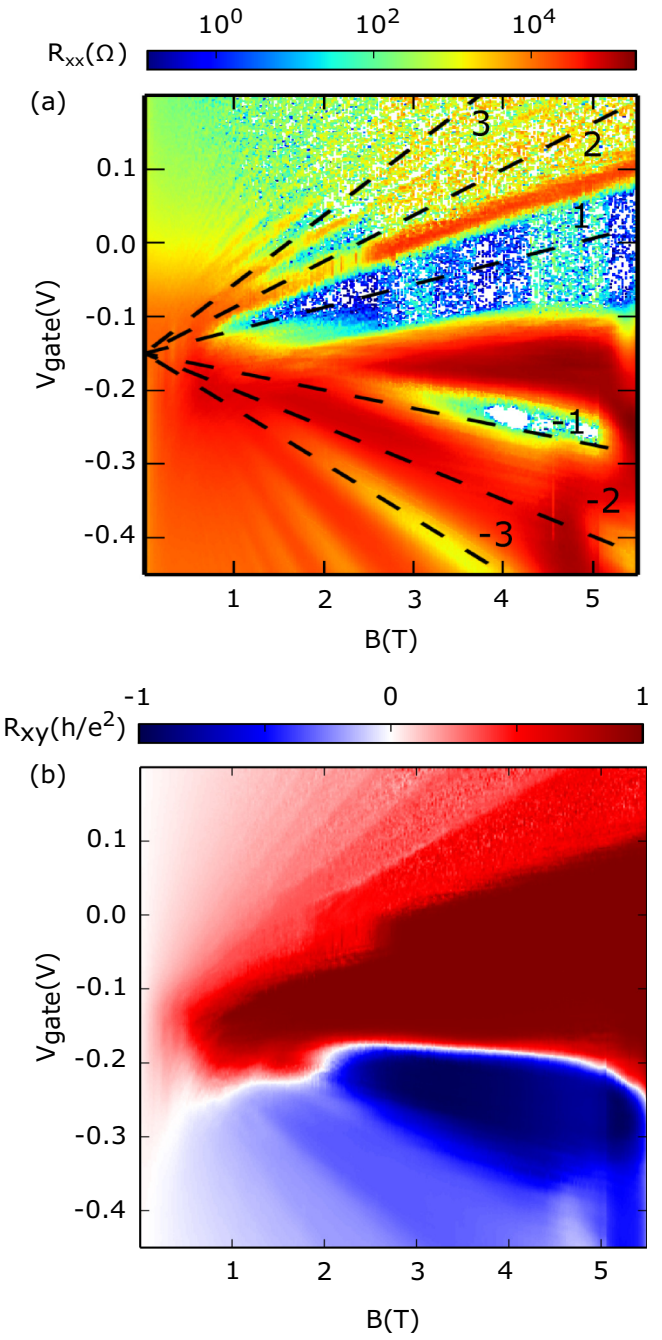

FIG. 9. (a) R_{xx} as a function of V_{gate} and the perpendicular magnetic field B. The black dashed lines represent the expected position of the minima of R_{xx} from the density evolution with V_{gate} extracted at low magnetic field (see Fig. 1). (b) Hall resistance R_{xy} (in units of $\frac{h}{e^2}$) as a function of V_{gate} and B. These data are extracted from sample 2.

APPENDIX B: MODEL AND ORIGIN OF THE LANDAU-LEVEL SPLITTING

1. Model

We consider a thin layer of topological insulator material, with two parallel surfaces indexed by $\tau^z = +1$ for the top (T) and $\tau^z = -1$ for the bottom (B) surface. The effective

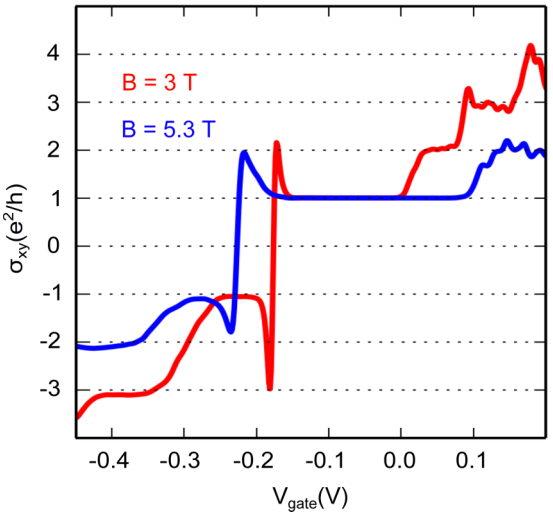

FIG. 10. Appearance of even filling factor on the hole side for high magnetic fields. Hall conductance σ_{xy} as a function of V_{gate} at $B = 3$ T (red) and $B = 5.3$ T (blue) for sample 2.

Hamiltonian for the surface states reads

$$H = v_f \tau_z \otimes (\hat{z} \times \vec{\sigma}) \cdot (-i\hbar\vec{\nabla}) + \left(\frac{\Delta}{2} + \frac{\hbar^2\nabla^2}{2M}\right)\tau_x \otimes \mathbb{I} + V\tau_z \otimes \mathbb{I}, \tag{B1}$$

where v_f is the Fermi velocity of the surface states and σ_x, σ_y describes Pauli matrices acting on the spin Hilbert space while τ_α acts on the T/B space. The first term describes the Dirac dispersion relation for the top and bottom surface states with opposite chirality (the spin winds in opposite ways around the Fermi surface), while $\Delta/2 - (\hbar k)^2/2M$ is a momentum dependent tunneling between the two surfaces, and V is the chemical potential difference between the surfaces. The band structure corresponding to this model is symmetric with respect to $E = 0$, and reads

$$E_\pm^2(\mathbf{k}) = \left(\frac{\Delta}{2} - \frac{\hbar^2 k^2}{2M}\right)^2 + (V \pm \hbar v_f |k|)^2. \tag{B2}$$

2. Landau spectrum

We consider a magnetic field B applied along z, perpendicular to the two surfaces. We obtain a spectrum with a chiral symmetry with respect to $E = 0$. The Zeeman coupling is neglected in the Hamiltonian (B1), so the effect of the magnetic field is purely orbital, and enters into the Hamiltonian by the minimal substitution $-i\hbar\vec{\nabla} \to -i\hbar\vec{\nabla} - e\vec{A}$ where $\vec{A}$ is the electromagnetic vector potential. In the gauge $(A_x = 0, A_y = Bx)$, we introduce the ladder operators

$$a = \frac{1}{\sqrt{2}}(q + ip);\ a^\dagger = \frac{1}{\sqrt{2}}(q - ip), \tag{B3}$$

$$q = \frac{X}{l_B} = \frac{x - k_y l_B^2}{l_B^2};\ p = -il_B\partial_X, \tag{B4}$$

where we introduced the magnetic length $l_B^2 = \hbar/eB$.

The Hamiltonian in the presence of a magnetic field can be rewritten as

$$H = -\eta\tau_z \otimes (a\sigma_- + a^\dagger\sigma_+) + \left(\frac{\Delta}{2} - \frac{\hbar\omega}{2}(2a^\dagger a + 1)\right)\tau_x \otimes \mathbb{I} + V\tau_z \otimes \mathbb{I}, \tag{B5}$$

where we introduced $2\sigma_\pm = \sigma_x \pm i\sigma_y$ and

$$\eta^2 = 2\frac{\hbar^2 v_f^2}{l_B^2} = 2\hbar v_F^2 eB; \quad \hbar\omega = \frac{\hbar^2}{Ml_B^2} = \frac{\hbar eB}{M}. \tag{B6}$$

We consider the basis $|N\rangle$ of quanta of the operators $a, a^\dagger$. In the basis $|T,\uparrow,N\rangle, |T,\downarrow,N-1\rangle, |B,\uparrow,N\rangle, |B,\downarrow,N-1\rangle$, the reduced Hamiltonian reads, for $N \geqslant 1$,

$$H_n = \begin{pmatrix} V, -\eta\sqrt{N}, \frac{\Delta}{2} - \frac{\hbar\omega}{2}(2N+1), 0 \\ -\eta\sqrt{N}, V, 0, \frac{\Delta}{2} - \frac{\hbar\omega}{2}(2N-1) \\ \frac{\Delta}{2} - \frac{\hbar\omega}{2}(2N+1), 0, -V, \eta\sqrt{N} \\ 0, \frac{\Delta}{2} - \frac{\hbar\omega}{2}(2N-1), \eta\sqrt{N}, -V \end{pmatrix} = \tau_x \otimes \left[\left(\frac{\Delta}{2} - N\hbar\omega\right)\mathbb{I} + \frac{\hbar\omega}{2}\sigma_z\right] - \eta\sqrt{N}\tau_z \otimes \sigma_x + V\tau_z \otimes \mathbb{I}. \tag{B7}$$

Its spectrum is symmetric with respect to 0 (chiral symmetric) and the energies satisfy

$$E_{N,\pm}^2 = V^2 + N\eta^2 + \left(\frac{\hbar\omega}{2}\right)^2 + \left(\frac{\Delta}{2} - N\hbar\omega\right)^2 \pm \left(N\eta^2[4V^2 + (\hbar\omega)^2] + (\hbar\omega)^2\left(\frac{\Delta}{2} - N\hbar\omega\right)^2\right)^{1/2} \text{ for } N \neq 0, \tag{B8}$$

which identifies exactly with the spectrum of [13] with the notation $B = \hbar^2/2M$.

In the case $N = 0$, we have to consider the basis $|T,\uparrow,0\rangle$ and $|B,\uparrow,0\rangle$. These basis states are annihilated by $a\sigma_-$ and by $a^\dagger\sigma_+$, and the effective Hamiltonian is then

$$H_0 = V\tau_z \otimes \mathbb{1} + \left(\frac{\hbar\omega - \Delta}{2}\right)\tau_x \otimes \mathbb{1}, \tag{B9}$$

with eigenvalues $\pm\sqrt{V^2 + (\hbar\omega - \Delta)^2/4}$.

3. Landau spectrum with $V = 0$

In the special case $V = 0$, we can rewrite Eq. (B8) as

$$\tilde{E}^2_{N,\pm} = N\eta^2 + \left(\frac{\hbar\omega}{2}\right)^2 + \left(\frac{\Delta}{2} - N\hbar\omega\right)^2 \pm \hbar\omega\left(N\eta^2 + \left(\frac{\Delta}{2} - N\hbar\omega\right)^2\right)^{1/2} = \left(\epsilon_N \pm \frac{\hbar\omega}{2}\right)^2, \tag{B10a}$$

$$\tilde{E}^2_0 = \left(\frac{\hbar\omega - \Delta}{2}\right)^2, \tag{B10b}$$

where

$$\epsilon_N = \left(N\eta^2 + \left(\frac{\Delta}{2} - N\hbar\omega\right)^2\right)^{1/2} \tag{B11}$$

Hence the degeneracy of the Landau levels ϵ_N of the two relativistic surfaces corrected by the nonrelativistic couplings is lifted by a splitting $\pm\hbar\omega/2$ ($\pm\beta$ in the notation of the main text). The $N = 0$ Landau level was initially not degenerate. Note that while this splitting is not of magnetic origin, it is linear in magnetic field, and can be viewed as an "effective Zeeman splitting" originating from the k^2 dependence of hybridization term between the top and bottom surfaces [13]. Such a Landau energy spectrum is represented in Fig. 7.

4. Nature of the "Landau-Level Splitting"

When $V = 0$ and in the limit $\Delta \to 0, \omega = 0$ the reduced Hamiltonian (B7) reads

$$H^{(0)}_N = -\eta\sqrt{N}\tau_z \otimes \sigma_x. \tag{B12}$$

The corresponding Landau eigenstates are (in the gauge we have chosen)

$$\psi^+_{N,+} = \frac{1}{\sqrt{2}}(|T,\uparrow,N\rangle - |T,\downarrow,N-1\rangle),$$
$$\psi^+_{N,-} = \frac{1}{\sqrt{2}}(|B,\uparrow,N\rangle + |B,\downarrow,N-1\rangle) \text{ for } \epsilon_N = \sqrt{N}\eta, \tag{B13a}$$

$$\psi^-_{N,+} = \frac{1}{\sqrt{2}}(|B,\uparrow,N\rangle - |B,\downarrow,N-1\rangle),$$
$$\psi^-_{N,-} = \frac{1}{\sqrt{2}}(|T,\uparrow,N\rangle + |T,\downarrow,N-1\rangle) \text{ for } \epsilon_N = -\sqrt{N}\eta. \tag{B13b}$$

They are entirely localized in either the top (T) or bottom (B) surface, and carry no net magnetization:

$$\langle\psi^+_{N,\pm}|S_x|\psi^+_{N,\pm}\rangle = \langle\psi^+_{N,\pm}|S_y|\psi^+_{N,\pm}\rangle = \langle\psi^+_{N,\pm}|S_z|\psi^+_{N,\pm}\rangle = 0. \tag{B14}$$

Let us now discuss the effect of various terms of the Hamiltonian (B7), treated as perturbations of the relativistic Landau Hamiltonian (B12):

(i) *Chemical potential asymmetry* V. The corresponding term is $+V\tau_z \otimes \mathbb{I}$ which merely shifts the energies of the Landau levels of the top surface with respect to those of the bottom surface without modifying their nature.

(ii) *Top/bottom hybridization*. The corresponding term is $(\frac{\Delta}{2} - N\hbar\omega)\tau_x \otimes \mathbb{I}$. This operator will shift the energies of the Landau levels and delocalize the eigenstates on both top and bottom surfaces but without any splitting between the two degenerate eigenstates. This can be inferred from the matrix elements,

$$\tau_x \otimes \mathbb{I}|\psi^\pm_{N,s}\rangle = |\psi^\mp_{N,s}\rangle \Rightarrow \langle\psi^+_{N,+}|\tau_x \otimes \mathbb{I}|\psi^+_{N,-}\rangle = 0. \tag{B15}$$

(iii) *Splitting*. the most striking consequence of the coupling between the two surface states arises from the k^2 term in (B1) and leads in the reduced Hamiltonian (B7) to a term

$$H_{\text{Splitting}} = \frac{\hbar\omega}{2}\tau_x \otimes \sigma_z, \tag{B16}$$

which satisfies

$$H_{\text{Splitting}}|\psi^+_{N,+}\rangle = |\psi^+_{N,-}\rangle. \tag{B17}$$

Indeed, while the two eigenstates $|\psi^+_{N,\pm}\rangle$ carry no magnetization, the spin and orbital degree of freedom (eigenstates N) are tightly bound together in their structure. This is illustrated by the absence of magnetization along x. It is this relation between spin and orbital degree of freedom which is broken by the perturbation $H_{\text{Splitting}}$, whose eigenstates are symmetric (S) or antisymmetric (A) between the two surfaces and read respectively for the positive and negative eigenvalues:

$$|\uparrow,S\rangle = \frac{1}{\sqrt{2}}(|T,\uparrow,N\rangle + |B,\uparrow,N\rangle),$$
$$|\downarrow,A\rangle = \frac{1}{\sqrt{2}}(|T,\downarrow,N-1\rangle - |B,\downarrow,N-1\rangle), \tag{B18a}$$

$$|\uparrow,A\rangle = \frac{1}{\sqrt{2}}(|T,\uparrow,N\rangle - |B,\uparrow,N\rangle),$$
$$|\uparrow,S\rangle = \frac{1}{\sqrt{2}}(|T,\downarrow,N-1\rangle + |B,\downarrow,N-1\rangle). \tag{B18b}$$

Note that these eigenstates carry a magnetization along z: the splitting of the Landau-level eigenstates will be associated with the appearance of finite magnetization along z of the eigenstates, linear in magnetic field (in ω).

[1] L. Fu, C. Kane, and E. Mele, Phys. Rev. Lett. **98**, 106803 (2007).
[2] J. E. Moore and L. Balents, Phys. Rev. B **75**, 121306(R) (2007).
[3] R. Roy, Phys. Rev. B **79**, 195322 (2009).
[4] D. Lee, Phys. Rev. Lett. **103**, 196804 (2009).
[5] C. Brüne, C. X. Liu, E. G. Novik, E. M. Hankiewicz, H. Buhmann, Y. L. Chen, X. L. Qi, Z. X. Shen, S. C. Zhang, and L. W. Molenkamp, Phys. Rev. Lett. **106**, 126803 (2011).
[6] D. A. Kozlov, Z. D. Kvon, E. B. Olshanetsky, N. N. Mikhailov, S. A. Dvoretsky, and D. Weiss, Phys. Rev. Lett. **112**, 196801 (2014).
[7] D. A. Kozlov, D. Bauer, J. Ziegler, R. Fischer, M. L. Savchenko, Z. D. Kvon, N. N. Mikhailov, S. A. Dvoretsky, and D. Weiss, Phys. Rev. Lett. **116**, 166802 (2016).
[8] B. Sacépé, J. Oostinga, J. Li, A. Ubaldini, N. Couto, E. Giannini, and A. Morpurgo, Nat. Commun. **2**, 575 (2011).
[9] Y. Xu, I. Miotkowski, C. Liu, J. Tian, H. Nam, N. Alidoust, J. Hu, C.-K. Shih, M. Hasan, and Y. Chen, Nat. Phys. **10**, 956 (2014).
[10] J. Linder, T. Yokoyama, and A. Sudbo, Phys. Rev. B **80**, 205401 (2009).
[11] C.-X. Liu, H. J. Zhang, B. Yan, X.-L. Qi, T. Frauenheim, X. Dai, Z. Fang, and S.-C. Zhang, Phys. Rev. B **81**, 041307(R) (2010).
[12] H.-Z. Lu, W.-Y. Shan, W. Yao, Q. Niu, and S.-Q. Shen, Phys. Rev. B **81**, 115407 (2010).
[13] S.-B. Zhang, H.-Z. Lu, and S.-Q. Shen, Sci. Rep. **5**, 13277 (2015).
[14] M. König, S. Wiedmann, C. Brüne, A. Roth, H. Buhmann, L. Molenkamp, X.-L. Qi, and S.-C. Zhang, Science **318**, 766 (2007).
[15] K.-M. Dantscher, D. A. Kozlov, P. Olbrich, C. Zoth, P. Faltermeier, M. Lindner, G. V. Budkin, S. A. Tarasenko, V. V. Bel'kov, Z. D. Kvon, N. N. Mikhailov, S. A. Dvoretsky, D. Weiss, B. Jenichen, and S. D. Ganichev, Phys. Rev. B **92**, 165314 (2015).
[16] P. Ballet, C. Thomas, X. Baudry, C. Bouvier, O. Crauste, T. Meunier, G. Badano, M. Veillerot, J. P. Barnes, P. Jouneau, and L. Lévy, J. Electron. Mater. **43**, 2955 (2014).
[17] O. Crauste, Y. Ohtsubo, P. Ballet, P. Delplace, D. Carpentier, C. Bouvier, T. Meunier, A. Taleb-Ibrahimi, and L. P. Lévy, arXiv:1307.2008.
[18] See appendix.
[19] V. Ariel, A. Natan, arXiv:1206.6100.
[20] Z. Jiang, Y. Zhang, H. L. Stormer, and P. Kim, Phys. Rev. Lett. **99**, 106802 (2007).
[21] A. J. M. Giesbers, U. Zeitler, M. I. Katsnelson, L. A. Ponomarenko, T. M. Mohiuddin, and J. C. Maan, Phys. Rev. Lett. **99**, 206803 (2007).
[22] K. Takase, H. Hibino, and K. Muraki, Phys. Rev. B **92**, 125407 (2015).
[23] Y. S. Gui, C. R. Becker, N. Dai, J. Liu, Z. J. Qiu, E. G. Novik, M. Schäfer, X. Z. Shu, J. H. Chu, H. Buhmann, and L. W. Molenkamp, Phys. Rev. B **70**, 115328 (2004).
[24] B. Büttner, C. X. Liu, G. Tkachov, E. G. Novik, C. Brüne, H. Buhmann, E. M. Hankiewicz, P. Recher, B. Trauzettel, S. C. Zhang, and L. W. Molenkamp, Nat. Phys. **7**, 418 (2011).
[25] M. König, H. Buhmann, L. W. Molenkamp, T. Hughes, C.-X. Liu, X.-L. Qi, and S.-C. Zhang, J. Phys. Soc. Jpn. **77**, 031007 (2008).
[26] P. Noël, C. Thomas, Y. Fu, L. Vila, B. Haas, P. H. Jouneau, S. Gambarelli, T. Meunier, P. Ballet, and J. P. Attané, arXiv:1708.05470.
[27] Note that these bands also possess edge states around the junction, which play a role only at very small magnetic fields before reaching the quantum Hall regime of interest in this paper.